Origin and regulation of oxygen redox instability in high-voltage battery cathodes

Xiang Liu[1,9], Gui-Liang Xu[1,9]*, Venkata Surya Chaitanya Kolluru[2,3], Chen, Zhao[1], Qingtian Li[4], Xinwei Zhou[2], Yuzi Liu[2], Liang Yin[5], Zengqing Zhuo[4], Amine Daali[1], Jing-Jing Fan[6], Wenjun Liu[5], Yang Ren[5], Wenqian Xu[5], Junjing Deng[5], Inhui Hwang[5], Dongsheng Ren[7], Xuning Feng[7], Chengjun Sun[5], Ling Huang[6], Tao Zhou[2], Ming Du[5], Zonghai Chen[1], Shi-Gang Sun[6], Maria K. Y. Chan[2], Wanli Yang[4]*, Minggao Ouyang[7]*, Khalil Amine[1,8]*

[1] Chemical Sciences and Engineering Division, Argonne National Laboratory, Lemont, IL 60439, USA

[2] Centre for Nanoscale Materials, Argonne National Laboratory, Lemont, IL 60439, USA

[3] Department of Materials Science and Engineering, University of Florida, 1885 Stadium Road, Gainesville, FL 32611, USA

[4] Advanced Light Source, Lawrence Berkeley National Laboratory, Berkeley, CA, USA

[5] X-ray Science Division, Argonne National Laboratory, Lemont, IL 60439, USA

[6] Department of Chemistry, Xiamen University, Xiamen 361005, China

[7] State Key Laboratory of Automotive Safety and Energy, Tsinghua University, Beijing 100084, China

[8] Materials Science and Engineering, Stanford University, Stanford, CA 94305, USA

[9] These authors contributed equally to this work

*Corresponding author. Email: xug@anl.gov; wlyang@lbl.gov; ouymg@tsinghua.edu.cn; amine@anl.gov

Abstract:

Oxygen redox at high-voltage has emerged as a transformative paradigm for high-energy battery cathodes by offering extra capacity beyond conventional transition-metal redox. However, it suffers from voltage hysteresis, voltage fade, and capacity drop upon cycling. Here, we show that, by eliminating the domain boundaries in the often-considered single-crystalline battery particles, layered oxide cathodes demonstrate exceptional capacity and voltage stability during high-voltage operation. Our combined experimental and theory studies for the first time reveal that the elimination of domain boundaries could enhance the reversible lattice oxygen redox while inhibiting the irreversible oxygen release, leading to significantly suppressed structural degradation and improved mechanical integrity during battery cycling and abuse heating. The robust oxygen redox enabled through domain boundary control provides practical opportunities towards high-energy, long-cycling, and safe batteries.

Main

High-energy batteries rely on high-capacity and high-voltage operation of the cathodes. Fundamentally, the capacity of a transition metal oxide-based cathode is determined by the amount of active Li, while the voltage is defined by the redox reactions affected by structural configurations[1]. This has led to two associated trends in recent cathode development: Li-excess compounds due to the large amount of Li (capacity) and oxygen redox (OR) at high-voltage[2-6]. However, intensive studies have shown that OR activities can trigger detrimental structural effects such as oxygen release, surface reactions, and phase transition, leading to severe voltage hysteresis, voltage fade, and poor capacity stability[3,5]. Despite extensive mechanistic understanding[3,5] and material optimization such as structural control[7-9], chemical composition manipulation[10], and cationic/anionic doping[11-13], the fundamental origin of the OR instability remains under active debate, and the practical control of high-voltage operation involving OR remains a formidable challenge. The key relies on a strategy that enhances the reversible OR in the lattice, while suppressing or even eliminating other detrimental oxygen activities.

Theoretical studies suggest that the surface could favour the migration of oxygen ions and promote the formation of oxygen vacancies due to the open atomic structure[14-16]. Therefore, surface-initiated irreversible oxygen loss and the associated structural transformation have long been considered as the root cause of the capacity decay and voltage fade of Li-excess layered cathodes when activating the OR process[16-18]. However, surface coatings to mitigate the oxygen loss have proven insufficient to achieve a fully reversible OR[5,18,19].

Grain boundaries (GBs), the surface that separates individual grains from each other, play a vital role in materials' properties. In layered oxide cathodes, the GBs have been predominantly

referred to the boundaries between primary particles of polycrystalline cathodes, while the so-called single-crystalline cathodes are free of these GBs and could thus overcome the cracking problem of polycrystalline cathodes during cycling within mild voltage range[20-23]. However, the reported "single-crystalline" cathode even with surface modification[22-30] still undergo visible capacity fading and voltage decay during high-voltage charge (e.g. $\geq$ 4.6 volts versus Li/Li^+) that will trigger OR[31,32], indicating that neither surface nor GBs is the origin of the OR instability. Recent studies have found that the often-considered "single-crystal" cathode grains, such as micro-crystalline $LiCoO_2$ and primary particles of polycrystalline NCM cathodes contain various types of sub grain boundaries (i.e. domain boundaries, denoted as DBs) such as low-angle tilt boundaries[33], twin boundaries[34], anti-phase boundaries[35] and etc. To date, the correlation between DBs and oxygen redox activity remain elusive, and the practical performance tuning through DBs engineering is lacking.

In this work, we provide a comparative study on four $LiNi_{0.6}Co_{0.2}Mn_{0.2}O_2$ cathodes deliberately synthesized to be DBs-free (denoted as BF-NCM) and, for comparison, a lab-synthesized single-crystalline cathode with increased internal DBs (denoted as N-NCM), a commercial single-crystalline cathode with increased internal DBs (denoted as C-NCM), and a DBs-rich $LiNi_{0.6}Co_{0.2}Mn_{0.2}O_2$ (denoted as BR-NCM) cathode with a surface coating. Through a series of spectroscopic, structural, and theoretical studies, we show that compared to the other three NCM cathodes with increased DBs, the DBs-free material (BF-NCM) displays an enhanced and reversible lattice OR at high voltages over a hundred cycles, but with the oxygen release eliminated. Therefore, BF-NCM cathode demonstrates exceptional capacity and voltage stability as well as negligible voltage hysteresis during high-voltage cycling.

Structures of the cathode materials

The morphologies of four NCM cathodes are shown in Supplementary Fig. 1, which reveals that BF-NCM, N-NCM and C-NCM cathodes exhibit similar "single-crystal" morphology, while BR-NCM presents typical structural features of polycrystalline cathodes. Synchrotron high resolution X-ray diffraction (HRXRD) (Supplementary Figs. 2A-2D) and the Rietveld refinement (Supplementary Tables 1-4) revealed that the all the cathodes exhibit a well-ordered hexagonal α-$NaFeO_2$ structure and similar Li/Ni mixing with no other impurity peaks. However, compared to the other three cathodes, BF-NCM shows smallest (003) peak broadening (Supplementary Fig. 2E) and microstrain (Supplementary Fig. 2F), which should be resulting from their distinct internal DBs structures. The high-angle annular dark-field scanning transmission electron microscopy (HAADF-STEM) image (Fig. 1A) and the corresponding elemental mapping (Fig. 1B) of BF-NCM indicate a uniform distribution of Ni, Co, Mn, and O. Moreover, the high-resolution HAADF-STEM image (Fig. 1C) and 4D-STEM nanobeam diffraction image (Fig. 1D) reveal the BF-NCM particle to be a single crystal without the presence of internal DBs. As a comparison, C-NCM exhibits significantly increased internal DBs although it shares similar outer morphology as BF-NCM (Supplementary Fig. 3).

Synchrotron Laue diffraction microscopy, which can determine the crystal orientation and strain/stress of crystalline materials (Supplementary Fig. 4), was employed to examine the crystallographic defects within BF-NCM, C-NCM and N-NCM particles. As shown in the crystallographic orientation map (Figs. 1E and 1F) and the lattice strain results (Supplementary Fig. 5), both two measured BF-NCM particles show very low degree ($< 0.5^{o}$) of misorientation and strain variation ($< 0.04\%$) throughout the particle, confirming the BF-NCM to be free of

DBs. By contrast, C-NCM particle (Fig. 1G) exhibits relatively large degree of misorientation (10°), while N-NCM particle (Fig. 1H) contains high density of adjunct subdomains with small degree of misorientation (~ 0.8°). In the case of BR-NCM, we found that it contains a surface Cr-enrichment structure to mitigate the effect of surface-induced degradation (Supplementary Fig. 6A). However, Supplementary Figs. 6B-6F clearly show that the primary particles are polycrystalline rather than the often-considered single crystals as often claimed. These structural features result in a poor structural stability of BR-NCM compared to BF-NCM (Supplementary Fig. 7).

Electrochemical performance of the cathode materials

These NCM cathodes were charging to a very high cut-off voltage of 4.7 V vs. Li/Li^+, corresponding to ~ 80% state of charge (SoC), in which 100% SOC is defined as extracting all the lithium to attain 274 mAh/g. Note that the OR activity is critical for determining the high-voltage performance of layered cathode materials[17,32]. As shown in Fig. 2A, BF-NCM cathode without DBs exhibited the best cycle stability amongst these four cathodes. It delivered a high initial specific capacity of 242.1 mAh/g on charge and 220.8 mAh/g on discharge (91% initial Coulombic efficiency) at C/3 rate (1C= 200 mA/g). After 100 cycles, a capacity retention as high as 97% was attained. By contrast, both N-NCM and C-NCM cathodes that possess increased DBs exhibited continuous capacity fading, with 60% and 83% capacity retention after 100 cycles, respectively. While the initial capacity of BR-NCM was slightly higher (249.5 mAh/g on charge and 227 mAh/g on discharge) than BF-NCM due to its smaller primary particle size[36], the capacity retention was much lower, at 88% after 100 cycles. These results have shown that the elimination of DBs is essential in improving cycling stability of NCM cathodes during high-

voltage operation. In addition, although surface doping can help to improve the high voltage cycling stability to some extent[37], it cannot prevent the structural degradation in the internal DBs (Supplementary Fig. 8). The comparison on the voltage stability shows that BF-NCM significantly mitigated the voltage hysteresis and voltage fade during aggressive cycling (Figs. 2B and 2C), indicating much less structural transformation during the OR. By contrast, N-NCM, C-NCM and BR-NCM cathodes all exhibit severe voltage decay with shifted capacity contribution from lower-voltage range (e.g., $\leq$ 3.6 V) (Figs. 2D-2F). The DBs-free BF-NCM cathode also outperformed the reported "single-crystal" NCM cathodes[22-30], which undergo obvious capacity degradation and intragranular cracking once charging to high voltage (Supplementary Table 5). This difference should be related to the inherently different DBs structures since they are both free of GBs. The reversible OR during high-voltage cycling of DBs-free NCM cathodes could enable ~30% energy density gain (higher specific capacity and average working voltage) compared to conventional NCM cathodes based on transition metal (TM) redox only (Supplementary Table 6). Such cathode innovation with robust TM cationic and oxygen anionic redox through DBs control is very encouraging because it leads to high energy density with no voltage hysteresis and voltage fade during cycling.

Characterization of cathodes during cycling or heating

To directly characterize the critical oxygen activities during high-voltage charge of NCM cathodes, we employed the oxygen K-edge ultrahigh-efficiency mapping of resonant inelastic X-ray scattering (mRXIS) technique with a probing depth of 100-200 nm. This technique can distinguish the intrinsic oxidized oxygen signals from strong transition metal characters that are entangled together in the O-*K* absorption spectroscopy[38], thus fingerprinting the OR activities in

both Li-excess and conventional as well as Na-deficient layered cathodes[5,7,13,31,38,39]. Technically, two associated mRIXS features represent the lattice oxidized oxygen: one at around 523.7 eV emission and 531 eV excitation energies[5,13,38], and the other at a low energy loss feature close to the elastic scattering around 531 eV excitation energy[40]. These features behave in the same way and are characteristic of the intrinsically oxidized oxygen states[41]. The intensity variation of these features provides a reliable evaluation of the OR upon electrochemical cycling[39]. Figs. 3A-3C show the O K-edge mRIXS of BF-NCM electrode at different charge/discharge states. As evident in Fig. 3A, the vertically extended broad features around 525 eV emission energy correspond to TM-O hybridization with TM 3d (below 535 eV excitation energy) and TM 4*s*4*p* (above 535 eV excitation energy). After charging to 4.8 V, this hybridization feature remains strong and further broadened due to the increased TM-O hybridization in the highly oxidized states. More importantly, the feature of lattice oxidized oxygen emerges around 531 eV excitation and 523.7 eV emission energies (red arrow in Fig. 3B), with an enhanced low energy loss feature close to the elastic line around the same excitation energy. When the electrode is discharged to 2.7 V, the features disappear, indicating a reversible OR in the BF-NCM cathode. Strikingly, the strong signal for lattice oxidized oxygen was well maintained and enhanced after 100 cycles (Fig. 3C). More importantly, this oxygen redox signature disappeared again at the 2.7 V discharged state of the 100th cycle, indicating that the oxygen redox is reversible over extended cycles of BF-NCM cathode (Supplementary Fig. 9). Although reversible OR reactions have been found in some cathode compounds for hundreds of cycles[39], the reaction always decays, as evidenced by the mRIXS feature decay upon cycling. This is the first time that clear signatures of enhanced OR have been found through extended cycles, directly implying the critical role of DBs in regulating the lattice OR in high-voltage battery cathodes.

For a direct comparison, the O K-edge mRIXS of the standard C-NCM cathode (Fig. 3D) shows the signature of the lattice oxidized oxygen when charging to 4.8 V, then disappears when discharged to 2.7 V, indicating a similar OR behavior to that of BF-NCM cathode during the initial cycle. However, after only 50 cycles, the intensity of the oxidized oxygen signal decreases significantly after the repeated charge/discharge process, indicating a fast decay of the OR reactions in contrast with that of BF-NCM.

For a detailed analysis, the integrated mRIXS intensity within the characteristic excitation energy window of 530.6 to 531.8 eV at different electrochemical states is plotted for BF-NCM and C-NCM cathodes. The characteristic signals of lattice OR start to emerge after 4.55 V, and get further enhanced at 4.8 V. Again, the intensity of lattice OR in the case of BF-NCM is enhanced after cycling (Fig. 3E). In sharp contrast, a clear decline on the OR intensity during cycling of C-NCM cathode was found (Fig. 3F).

In the case of BR-NCM with surface Cr-enrichment, the intensity of the OR feature at the 1st 4.8V-charge state is much weaker (Supplementary Fig. 10), indicating a limited lattice OR activity in the BR-NCM cathode. After 100 cycles, a finite amount of OR feature could be seen. The slight enhancement of the OR feature upon cycling should be due to the surface Cr-enrichment on the BR-NCM particles. Surface modification indeed helps in sustaining the lattice OR to some extent, as expected before and revealed here [**Citations needed here?**]. It is important to note that, for Li-ion battery cathodes, only Li-rich electrodes have been found previously to have strong OR reactions over hundreds of cycles [Cite Gent et al., Nat Comm 8, 2091, 2017 10.1038/s41467-017-02041-x here if possible]; however, recent clarifications have suggested that the Li-rich configuration itself is also the culprit of of irreversible and detrimental

oxygen oxidation [Cite Zhuo et al., Joule 5, 975, 2021, doi 10.1016/j.joule.2021.02.004 here if possible], but conventional NCM cathode materials themselves display only a fast decay of the OR[32]. Therefore, the finding here on the reversible OR over a hundred cycles in conventional cathode is nontrivial and suggests the critical effect of boundary controls towards to sustain the lattice OR upon extended cycles over other methods.

In-situ differential electrochemical mass spectroscopy (DEMS) characterization (Supplementary Fig. 11) revealed that no oxygen release was observed for the BF-NCM cathode, whereas BR-NCM cathode undergoes an obvious oxygen release starting at 4.55 V. In many OR systems, the activated oxygen typically leads to the emergence of both oxygen release and lattice oxygen redox[42]. In sharp contrast, BF-NCM that is free of DBs display exactly the opposite behaviour, i.e., enhanced lattice oxygen redox reactions (Fig. 3) but suppressed oxygen release. The DEMS results clearly suggest that DBs control could bypass the detrimental part of the oxygen activities on the irreversible reactions. Other than practical optimization, this also indicates that the reaction mechanism of these two kinds of oxygen activities may be fundamentally different[13,42], and thus could be controlled separately through DBs tailoring.

The contrast on the oxygen release amongst different cathodes was further confirmed by synchrotron X-ray absorption of TM K-edge spectra at different SoC (Supplementary Fig. 12A and 12B). As shown, both Ni and Co undergo an obvious edge shift towards lower energy when further charging the BR-NCM cathode from 4.55 V to 4.8 V, corresponding to the valence decrease of Ni and Co at high-voltage (Supplementary Figs. 13A-13D). Similar results can be found in the case of C-NCM cathode during charging from 4.55 V to 4.80 V (Supplementary Fig. 14). The observed O_2 release by DEMS is one of the critical reasons, which could cause the

reduction of Ni and Co due to charge balance. Similar phenomena of O_2 release-induced TM reduction were also observed during repeated cycling of Li-rich cathode[17] [If you cite the 2021 Joule doi 10.1016/j.joule.2021.02.004 above, you may cite it here. It's the extreme case of Li-rich showing that system does not work, so conventional compounds is the way to go and to optimize], and during heating of delithiated NCM cathodes[43]. Meanwhile, other undesired processes such as proton insertion[44] and formation of rock-salt phase (e.g., NiO) with lower valence state could also lead to valence decrease of TM. In comparison, no visible edge shift (Supplementary Fig. 12C and 12D) and no TM valence reduction (Supplementary Figs. 13E-13H) can be observed in the case of the BF-NCM cathode, indicating significantly less structural deformation.

In-situ high-energy X-ray diffraction (HEXRD) was further used to investigate the bulk phase transformation of NCM cathodes during charge/discharge. Overall, BF-NCM demonstrates suppressed structural transformation in comparison with BR-NCM, in particular, at the high-voltage region (Figs. 4A and 4B). The (105) peak shifts to a higher angle during extraction of Li^+ due to the TM oxidation, resulting in the contraction of the TM-O bond and decrease of the *a* lattice parameter (Supplementary Fig. 15). The (003) peak shifts to lower angle in low-voltage regions during delithiation. The repulsion between adjacent oxygen planes increases during charge and leads to an increase of the *c* lattice parameter and shift of (003) peak. Starting at 4.3 V, the (003) peak shifts back to higher angles and indicates a contraction of the *c* parameter at high SoC. The underlying mechanism for such contraction during deep charge remain under active debate, either due to 'lattice collapse' phenomenon[45,46] or appearance of "two-phase" processes at high SoC of layered cathode[47].

The participation of oxygen oxidation at high SoC of layered cathodes, as confirmed by

mRIXS characterization in this work, may explain these phenomena, which can cause the dissipation of the effective charge on oxygen and hence gradual contraction between oxygen planes. If the oxygen atoms are transferred into an oxygen singlet, oxygen vacancies, or other oxygen-depletion structures, the effective repulsion force between oxygen planes will decline and lead to the severe contraction of the layered structure along with decrease of TM valence state (Supplementary Figs. 13A-13D) and increase of *a* parameter during deep charge (Supplementary Fig. 15A). As shown in Figs. 4C and 4D, the layer structure of BF-NCM was still well maintained even when charging to 4.7 V, while substantial peak broadening and an asymmetry peak feature occurred at high SoC of BR-NCM, indicating the presence of multiple phases. High-resolution X-ray diffraction (HRXRD) detected a trace amount of crystallite phases, and the Rietveld refinement (Supplementary Fig. 16 and Supplementary Table 7) revealed that no new phases were formed in the BF-NCM after triggering the OR. In contrast, spinel-like peaks were detected in the BR-NCM after charging to 4.8 V (Supplementary Figs. 17 and 18). The Rietveld refinement (Supplementary Table 8) clearly showed that about 3.5 mol% of the TM cations migrated from octahedral sites to interstitial tetrahedral sites and formed a spinel-like phase in the BR-NCM.

These results were further elaborated by probing the structural transformation and gas evolution of charged cathodes during abuse heating, which undergo similar structural response as that during normal charge/discharge, but at a much faster speed[17]. Figs. 4E-4G and Supplementary Fig. 19 show that the charged BR-NCM, BF-NCM and C-NCM cathodes all exhibited typical phase transformation of charged layered cathodes during heating: from layered structure (R-3m) to spinel structure (Fd3m) to rock-salt (Fm-3m)[43]. The critical temperature for

maximal oxygen release for charged BR-NCM, C-NCM and BF-NCM cathode are 292 °C, 361 °C, and 412 °C, respectively. The results indicated that DBs-free BF-NCM present the best oxygen stability during abuse heating. In addition, charged BF-NCM exhibited a higher temperature (253°C) for the shift of the (003) peak than that of the charged BR-NCM (231°C), indicating that charged BF-NCM can better constrain TM ions in the 3*a* octahedra sites and hence suppress their migration (Supplementary Fig. 20). As confirmed by the Arrhenius method[48], the oxygen release kinetic barrier of charged BF-NCM is > 3 times higher than that of charged BR-NCM (Supplementary Fig. 21).

The structure stability was further examined by comparing the lattice reversibility during heating/cooling (Fig. 4H). Irreversible TM migration in charged BR-NCM occurred beyond 190 °C, leading to irreversible phase transition after cooling and increase of microstrain and further microcracking (Supplementary Figs. 22A-22D, and Supplementary Fig. 23), which, in turn, aggravate oxygen release and structural degradation. By contrast, the charged BF-NCM cathode showed excellent lattice reversibility, leading to no permanent lattice oxygen loss, no TM migration, and thus better structural integrity (Supplementary Figs. 22E-22H, and Supplementary Fig. 24). Therefore, charged BF-NCM exhibited less transition metal reduction upon heating (Supplementary Figs. 25 and 26). These results have confirmed the robust oxygen-loss tolerance of charged BF-NCM. This led to its improved safety performance compared with the BR-NCM cathode in practical pouch cells (Supplementary Fig. 27).

DFT simulation on oxygen stability and domain boundaries

The OR behaviour of layered cathodes with distinct DBs structures is illustrated schematically in Figs. 5A and 5B. Upon activation of oxygen oxidation at high SoC, the existence

of high-density DBs could facilitate the formation and migration of oxygen ions/vacancies, thereby promoting irreversible oxygen loss. Indeed, fast ion migration kinetics at the boundaries is known for many other energy-related materials[49,50]. Thus, non-lattice OR dominates in the DBs-rich cathodes during high-voltage charge.

This hypothesis was supported by density functional theory (DFT) calculations (see Methods section for details) on the tilt boundary structural models, which include fully lithiated ($Li_3NiCoMnO_6$) and partially delithiated ($Li_{0.375}NiCoMnO_6$), obtained from HAADF-STEM image[33]. We performed structural relaxation of the two initial DBs structures and found that, upon relaxation, one-dimensional (1D) channels of TM vacancies are formed along the plane of the DBs in the fully lithiated structure (Fig. 5C). Whereas the oxygen atoms at the DBs of the delithiated structure possess dangling bonds (Fig. 5D). We further consider twin boundary structural models, both fully lithiated ($Li_3NiCoMnO_6$) and partially delithiated ($Li_{0.357}NiCoMnO_6$) (Figs. 5F and 5G) to understand the OR behaviour in a DB structure with relatively well-coordinated oxygen atoms at the DB interface region.

The oxygen atoms at the domain boundaries (DBs) show differences in oxygen vacancy formation free energies related to their local bonding environment. To map the free energies and local environments of different oxygen sites near the interface region, we divide them into four sets S1, S2, S3 and S4 along the *b*-lattice vector. Within each set, the oxygen atoms are shown in different colours (red, orange, green, cyan, brown, magenta). The local environment of different oxygen atoms can be observed in the structural models (Figs. 5C, D, F, G, Supplementary Figs. 28 and 29) with corresponding vacancy free energy (circles) and net charge (triangles) are shown in Fig. 5E and Fig. 5H respectively with the same colour within different sets. Within each set, the

solid markers correspond to fully lithiated DBs whereas empty filled markers correspond to partially delithiated DBs. The red (~ 2.1 eV) and blue (~ 0.04 eV) dotted lines correspond to the oxygen atoms in the bulk supercells, and the filled and empty circles correspond to those at the DBs of fully lithiated and partially delithiated structures, respectively.

We notice that the vacancy formation free energies for the fully lithiated structures are higher than those of the partially delithiated structures and are strongly correlated to the net charge on the respective oxygen atoms. The more negative the net charge on oxygen sites, the more stable it is (i.e., the higher vacancy formation free energy). At high SoC conditions (partially delithiated DBs), along with increased configurational entropy, the net charge on oxygen atoms becomes less negative (see the empty triangles) due to weakened TM-O bonds, indicating that these oxygen atoms are oxidized during charge. This lowers the vacancy formation free energy (see the empty circles) during charge. While the above analysis concerns only the thermodynamics of oxygen evolution and does not tackle the kinetics, the presence of open 1D channels along the DB plane also suggests a lower barrier for diffusion of oxygen atoms along the DBs compared to that in the bulk.

We observe similar trends in both tilt and twin boundary DBs corresponding to free energies of vacancy formation and net charge. The bonding environment for different oxygen sites in the fully lithiated twin DB structure is more homogeneous compared to that in the high-angle DBs, leading to higher oxygen vacancy formation energy for different oxygen sites. Whereas the oxygen sites in the partially delithiated twin DB have different local bonding environments. Particularly, the oxygen vacancy formation energies became negative, indicating the thermodynamically unstable nature of oxygen atoms even at the twin boundary. The results from

both tilt and twin DBs, containing very diverse coordination environments, suggest that the stability of oxygen at the DBs corresponds to the local coordination and net charge of the oxygen atoms. While it is not possible to model all possible boundaries, the results suggest a general observation that under-coordinated oxygen atoms at DBs become unstable, particularly at high SoC conditions.

Conclusion

In summary, our observation of robust and even enhanced oxygen redox in the DBs-free layered cathodes during prolonged cycling supports the critical role of DBs in modulating the oxygen redox behaviour. This enables the selective enhancement of the lattice OR while suppresses the oxygen release, achieving the oxygen activity control for high-voltage battery cathodes over a hundred of cycles in conventional materials. This intriguing finding can significantly increase the energy density of state-of-the-art battery cathode technology without sacrificing the cycle life, energy efficiency, and safety performance, as directly demonstrated in this work. Open questions remain on the fundamental mechanism of the much improved OR sustainability, and this work will trigger tremendous interest in both fundamental understanding and practical optimization through tailoring the DBs structure in cathodes from synthesis strategies and boundary engineering.

Methods

Materials. BF-NCM and BR-NCM cathodes were both provided by Beijing Easpring Material Technology Ltd., Beijing, China, while C-NCM was a commercial single-crystal cathode purchased from another vendor. Typically, $Ni_{0.6}Co_{0.2}Mn_{0.2}(OH)_2$ precursor was synthesized by a co-precipitation method using 50 L reactor set at 55 ^{o}C. The transition sulfate solution

(Ni:Co:Mn=0.6:0.2:0.2 in molar ratio, 2 mol/L), 10M NaOH and 5 mol/L $NH_3 \cdot H_2O$ were fed into the tank, respectively. The pH value was control at 11.6 during co-precipitation process by adjusting NaOH feeding rate. The synthesized $Ni_{0.6}Co_{0.2}Mn_{0.2}(OH)_2$ precursor was obtained by filtering and washing with DI water and drying at 105 °C for 8 hours.

BF-NCM: The hydroxide $Ni_{0.6}Co_{0.2}Mn_{0.2}(OH)_2$ precursor and lithium oxide ($LiOH \cdot H_2O$) was mixed at 1:1.08 molar ratio (TM:Li=1:1.08). Then the mixture was sintered at 920 °C for 10 hours with 10 °C/min ramping rate in oxygen atmosphere, followed by nature cooling down. The sintered products then jet pulverized and finally re-calcinated at 600 °C for 5 h at 10 °C/min to get the BF-NCM cathode.

BR-NCM: The hydroxide precursor and lithium oxide ($LiOH \cdot H_2O$) was mixed at 1:1.08 molar ratio (TM:Li=1:1.08). With the weight ratio of Cr at 50 ppm (0.005%) (for example, 73.1mg Cr_2O_3 added in 1kg NCM precursor during calcination), the Cr_2O_3 was added as the source materials as a surface dopant to enhance the surface stability. These mixtures were then sintered at 850°C for 10 hours using 10 °C/min ramping rate in oxygen atmosphere. The sintered products were then the post annealing at 600 °C (10 °C/min ramping) for 5 hours in oxygen atmosphere was carried out before collecting end products of BR-NCM.

N-NCM cathode with increased domain boundaries were prepared similarly by a high-temperature calcination method. The $Ni_{0.6}Co_{0.2}Mn_{0.2}(OH)_2$ precursor was mixed with $LiOH \cdot H_2O$ at a mole ratio of Li: transition metal = 1.08:1. Then, the calcination process was carried out in a tube furnace with pure oxygen atmosphere at 920 °C for 20 h with a heating rate of 5 °C/min and cooling rate of 2 °C/min.

Morphology characterization. The morphologies of the samples were characterized by scanning

electron microscopy (SEM, JSM-7100F, JEOL) and transmission electron microscopy (FEI F200X and JEOL 2100F). To investigate the inner structure of the cathode particles, cross-sectional samples were prepared with a focused ion beam-scanning electron microscopy dual-beam system (Zeiss Nvision 40).

High-resolution X-ray diffraction (XRD). The high-resolution XRD data for the pristine and charged cathode materials were obtained with 12-detector synchrotron X-ray diffraction at Beamline 11BM (λ=0.412836 Å) of the Advanced Photon Source (APS), Argonne National Laboratory. The data acquisition parameter was 0.001 degree per step with 0.1 s.

High-energy X-ray diffraction (HEXRD). For the in-situ heating and cooling, the charged cathode was collected in a glovebox with dimethyl carbonate rinsing and vacuum drying from a pouch cell that had been charged to 4.2 V. In-situ HEXRD during charge/discharge cycling and in-situ HEXRD during heating/cooling of the 4.2 V (vs. graphite) charged cathode were obtained at Beamline 11 ID-C of the APS with a wavelength of 0.1173 Å. A Linkam TS1500 stage furnace was used to heat the cathode powder at 2 ^{o}C/min to 210 ^{o}C and then to cool at the same rate to 30^{o}C. The in-situ HEXRD was conducted in half-cells with BF-NCM or BR-NCM cathodes and lithium metal anode. Charge/discharge was conducted with a constant rate of C/10 between 3.0 V and 4.7 V. The PerkinElmer amorphous silicon 2D detector was used to collect the diffraction patterns, then patterns were calibrated by a standard CeO_2 sample and finally converted to 1D patterns using GSAS II software. Rietveld analysis with the GSAS II program was used to refine the high-energy diffraction patterns and to thereby monitor the in-situ lattice parameter evolution.

Differential electrochemical mass spectroscopy (DEMS). DEMS experiments were conducted in a custom-made system. A slurry consisting of 80 wt. % active materials, 10 wt. % PVDF binder,

and 10 wt. % conductive carbon, was coated on a 16-mm diameter carbon paper and then dried (loading mass of active material was around 10 mg/cm^2). A 2025-coin cell with hole was assembled with a lithium metal anode and Celgard 2400 separator. The coin cell was charging/discharging at 2.7-4.8 V and a current density of 45.6 mA/g. Pre-dehydrated helium (99.999%) was used as the carrier at a flow rate of 8 mL/min. The gas species during the charge/discharge were passed through a cold trap (mixture of dry ice and ethanol at -78.5 °C and 1 atm) to condense the electrolyte vapor before it enters the mass spectrometer (modified 5975C mass-selective detector, Agilent).

In-situ HEXRD during heating with mass spectrometry (MS). A home-made time-resolved HEXRD system was utilized in Beamline 17-BM at the APS to characterize the phase transformation during heating, with X-ray wavelength of 0.24125 Å. The 4.2-V charged (vs. graphite) cathode powder was collected from a pouch cell or coin cell and loaded into a quartz capillary tube with controllable heating equipment. Ultra-high purity argon was used as the carrier gas, and a RGA residual gas analyser (PrismaPlus, QMG 220) was utilized to measure the gas evolution. The heating rate was 10 °C/min from room temperature to 600 °C, and the HEXRD data rate was about 1 min/image with a 2D detector. The HEXRD data were converted and analysed with GASA II software.

Electrochemical test. The active material was mixed with acetylene black and PVDF (92:04:04 in weight ratio) in *N*-methyl-2-pyrrolidone to prepare the cathode laminates. Then the slurry was casted onto Al foil and dried in a vacuum oven at 75 °C overnight. The loading of active material in the electrode was controlled at ~ 4 mg/cm^2. 2032-type coin cells were used to evaluate the electrochemical performance with a lithium metal as anode, a Celgard-2025 as separator, and 1M

$LiPF_6$ in ethylene carbonate and ethyl methyl carbonate (3:7 by volume) as electrolyte without additives. Cell assembly was performed in a glove box filled with argon, where the moisture and oxygen content were controlled below 1 ppm. A MACCOR battery testing system was utilized for the cycling performance measurement, and the cells were charging and discharging within 3.0-4.7 V (BF-NCM and BR-NCM) or 2.7-4.7 V (C-NCM and N-NCM) by applying a constant rate of C/3 at room temperature.

X-ray absorption spectroscopy (XAS). To reveal the local structure evolution of cycled or heated cathodes, XAS characterization was characterized at Beamline 20-BM of the APS. A Linkam THMS600 stage furnace was used to heat the charged cathode from 30 ^{o}C to 300 ^{o}C at a rate of 2 ^{o}C/min. The Ni K-edge data were continuously collected during the heating. Extended X-ray absorption fine structure (EXAFS) data were extracted and normalized with established methods using the ATHENA software package, and the EXAFS data in the region of 1.2-3.5 Å were fitted in the r-space to the theoretical EXAFS calculation with the ARTEMIS software package.

Synchrotron Laue diffraction microscopy. Synchrotron Laue diffraction measurements were conducted at Beamline 34-ID-E of the APS. The BF-NCM, N-NCM and C-NCM samples were uniformly dispersed on a silicon nitride membrane window. A polychromatic or monochromatic X-ray microbeam (7-30 keV) was focused by using two Kirkpatrick-Baez mirrors to a size of 250 nm, where the Laue diffraction patterns were recorded on a PerkinElmer area detector. The crystal orientation map was required in the polychromatic mode with an accuracy of 0.01°, while the absolute lattice parameters and local elastic lattice strains inside individual domains were quantitatively measured in the monochromatic energy-scanning mode with an accuracy of $1x10^{-4}$. Scanning step size of 250 nm was used for all the mappings.

O K-edge resonant inelastic X-ray scattering (RXIS) characterization. The O K-edge RIXS characterization was performed at Beamline BL8.0.1 of the Advanced Light Source at Lawrence Berkeley National Laboratory[51]. To avoid any air exposure, all electrode samples were handled carefully in a high purity argon glove box and then transferred to the beamline station via an airtight transfer mini-chamber. The measured sample was mounted 45° to the incident beam, and the emitted photon was collected at 90° to the incident photon with the emission energy resolution of 0.25 eV on the O K-edge through the spectrograph[52]. All energies in the RIXS results were calibrated by measuring TiO_2 reference samples to adjust the first main peak of O-K XAS at 531 eV, and all RIXS data were processed in a six-step procedure and normalized to the incident beam flux, with technical details explained elsewhere[53]. Key samples, such as the fully charged cathode with different cycles, were measured on multiple freshly prepared samples. The electrode materials were collected by disassembling coin cells in the glovebox right after charging at the target voltage with constant current mode of C/10 and constant voltage charge for 10 hours. The samples in the discharge state were collected right after discharge to the target voltage at C/10 with no constant voltage mode.

X-ray ptychography. X-ray ptychography was performed on the Velociprobe[54] located at Beamline 2-ID-D of the APS. An 8.33-keV monochromatic X-ray beam was focused by a Fresnel zone plate with an outermost zone width of 50 nm. The sample was placed 500 μm downstream of the focusing position of the zone plate, with an illumination size of about 1.2 μm. Both BF- and BR-NCM particles were placed on Si_3N_4 windows with a membrane thickness of 200 nm. As the sample was raster-fly scanned, a Dectris Eiger 500K hybrid pixel array detector (2.335 m downstream of the sample) collected forward coherent diffraction patterns at a continuous frame

rate of 100 Hz. For ptycho-tomography data collection of the BF-NCM particles, the sample was rotated by 1° angular increment, covering an angular range from -63° to 77°; for the BR-NCM particles, the sample was rotated by 0.5° increment for an angular range from -60° to 64°. 2D ptychography projections were reconstructed with a real-space pixel size of 9 nm by a GPU-based code[55]. The obtained 2D projections were aligned by cross correlation to a common rotation axis, and tomography reconstructions were carried out by a simultaneous iterative technique using the ASTRA toolbox through its interface provided in Tomopy[56].

Pouch cell fabrication and Accelerating rate calorimeter (ARC) testing. Pouch cells (1-Ah level) were fabricated with either a BR-NCM or BF-NCM cathode and artificial graphite anode with the same configuration. The cathode consists of 94 wt.% BF-NCM or BR-NCM cathode, 2 wt.% polyvinylidene fluoride (PVDF), and 4 wt.% conductive carbon. The anode consists of 96 wt.% artificial graphite, 2 wt.% carbon black, and 2 wt.% sodium carbon methylcellulose and styrene butadiene rubber binder. The electrolyte is 1 M $LiPF_6$ in ethylene carbonate, propylene carbonate, and diethyl carbonate in 1:1:1 volume ratio. The negative-to-positive electrode ratio for the pouch cell is around 1.1.

For thermal runaway characterization, ARC tests were conducted using an EV^+ ARC (Thermal Hazard Technology) system with the pouch cells. For each ARC test, two identical fully charged pouch cells were combined with a thermocouple in between. The starting temperature was 40 °C with a heating step of 5 °C. The ARC was conducted in a typical heat-wait-seek mode, with the detected self-heating rate at 0.02 °C/min and a waiting time of 40 min. Before the test, the ARC system was calibrated to adiabatic between 40 °C to 300 °C with an Al brick as a battery substitute. A drift experiment was conducted after calibration to confirm the system reliability.

Density functional theory (DFT) calculations. We performed DFT calculations on the tilt and twin domain boundary structures. We used the "ingrained" package[57]. we developed to obtain the domain boundary structure. Ingrained is an automated python package that uses the information regarding the orientation of the top and bottom grains constituting the domain boundary to provide an initial domain boundary structure. The input parameters for "ingrained" include the composition ($Li_3MnCoNiO_6$), hkl-upward [010], hkl-projected [001], tilt angle of the top domain (-71°), and bottom domain (38°) perpendicular to the hkl-projected axis that corresponds to the alignment of respective domains. The simulated HAADF-STEM image (Supplementary Fig. 30) of the computed boundary matches well with the previously reported experimental HAADF-STEM image of layered cathodes[33]. The twin boundary structure was simulated according to the previous work by He et al.[58] The software imports the bulk structure from the Materials Project database[59,60] and creates a domain boundary structure by aligning the slabs of the top and bottom domains. We reduced the domain boundary structure to ~15 Å thickness to be computationally efficient. We performed structure relaxation of the fully lithiated domain boundary structure in order to optimize the cell shape along with atomic positions. To create the delithiated structure, we remove lithium atoms from the optimized structure to maintain required concentration (~12.5% Li) comparable to the BF-NCM and BR-NCM samples and perform a Monte Carlo search with only electrostatic forces using the GULP software[61].

We found a low energy configuration of the remaining 6 (or 5) Li atoms within the tilt (or twin) boundary structure and relax this low lithium DB structure by fixing the cell shape, and only relax atoms near the plane of the DB. This ensures that the structure remains intact – the angle between the two grains and the simulated TEM image are comparable to the experimental TEM

image. DFT calculations are performed on both the fully lithiated and partially delithiated tilt and twin domain boundary structures, and corresponding bulk supercells to compare the oxygen vacancy formation energies in different local environments. We performed DFT calculations to determine free energies for oxygen vacancy formation by removing an oxygen atom from all the 24 and 12 different sites near the interface region of the relaxed tilt boundary and twin boundary structures respectively and from the 2x2x2 supercells of both the corresponding bulk structure. We used the plane wave DFT code VASP[62,63] with PBE PAW atom potentials[64,65] for lithium and transition metals, and the soft potential for oxygen. We chose a plane wave energy cut-off of 353.6 eV, and an automatic k-point mesh with 30 k-points per $Å^{-1}$. We used Gaussian smearing with a width of 0.05 eV. We perform Bader analysis to observe the net charge on different oxygen sites in the fully lithiated and partially delithiated structures of both the tilt and twin boundary structures.[66]

The chemical potential of oxygen μ_O at room temperature was obtained from the enthalpy of formation (DH) of solid-state lithium oxide (Li_2O), in a modification of the procedure first introduced in the literature[67] to correct for the PBE error in oxygen molecule energy.

$$\Delta H^{\square}_{Li_2O(s)} = E_{Li_2O(s)} - 2E_{Li(s)} - \mu_O \qquad \text{Equation (1)}$$

where $E_{Li2O(s)}$ and $E_{Li(s)}$ are the total energies of solid state Li_2O and Li metal from DFT calculations. The oxygen vacancy formation free energy is then obtained from:

$$\Delta G_O^{vac} = E_{db-O} - E_{db} + \mu_O - T\Delta S \qquad \text{Equation (2)}$$

where E_{db} and $E_{db\text{-}O}$ are the energies of the relaxed domain boundary structure and the DB structure with an oxygen vacancy, respectively; and TDS is the entropic contribution at 300 K, taken as approximately the entropy of gaseous O_2[68].

Acknowledgements: The authors acknowledge the helpful discussion of DFT simulation on the oxygen redox behaviour of boundary-tailored layered cathodes with Prof. Gerbrand Ceder at the University of California, Berkeley, and Lawrence Berkeley National Laboratory. The authors acknowledged Dr. Barry Lai at Advanced Photon Source of Argonne National Laboratory for the technical support on the Ptychography characterization.

Funding: Research at the Argonne National Laboratory was funded by the U.S. Department of Energy (DOE), Vehicle Technologies Office. Support from Tien Duong of the U.S. DOE's Office of Vehicle Technologies Program is gratefully acknowledged. Use of the Advanced Photon Source (APS) and the Centre for Nanoscale Materials, both Office of Science user facilities, was supported by the U.S. Department of Energy, Office of Science, and Office of Basic Energy Sciences, under Contract No. DE-AC02-06CH11357. XL, GLX, MO and KA thank the support from Clean Vehicle Consortium, US-China Clean Energy Research Centre (CERC-CVC2).

Author contributions: GLX and KA initiated and supervised the project. GLX and XL conceived the idea and designed the experiments. XL and CZ carried out the electrochemical tests. XL, LY, AD, YR, and ZC carried out in-situ and ex-situ XRD measurements and analysis. XL conducted the in-situ heating HEXRD and mass spectroscopy with the assistance of WX. QL, ZZ and WY conducted the RIXS characterization and analysis on the samples prepared by XL and CZ. WL conducted synchrotron X-ray Laure diffraction characterization and analysis. XZ, YL and TZ performed the SEM and TEM characterization and analysis. DR and XL performed the ARC test. XL and XF carried out the TGA-MS test with different temperature rates under the supervision of MO. XL, IH and CS performed the XAS measurement and analysis. JD performed X-ray ptychography characterization and analysis with the help of MD. JF

conducted the DEMS under the supervision of LH and SGS. VSCK and MKYC performed DFT calculations. GLX, XL and WY wrote the manuscript with input from all authors.

Competing interests: The authors declare no competing interests.

Data and materials availability: The data supporting the findings of this study are available within the article and its Supplementary Information files.

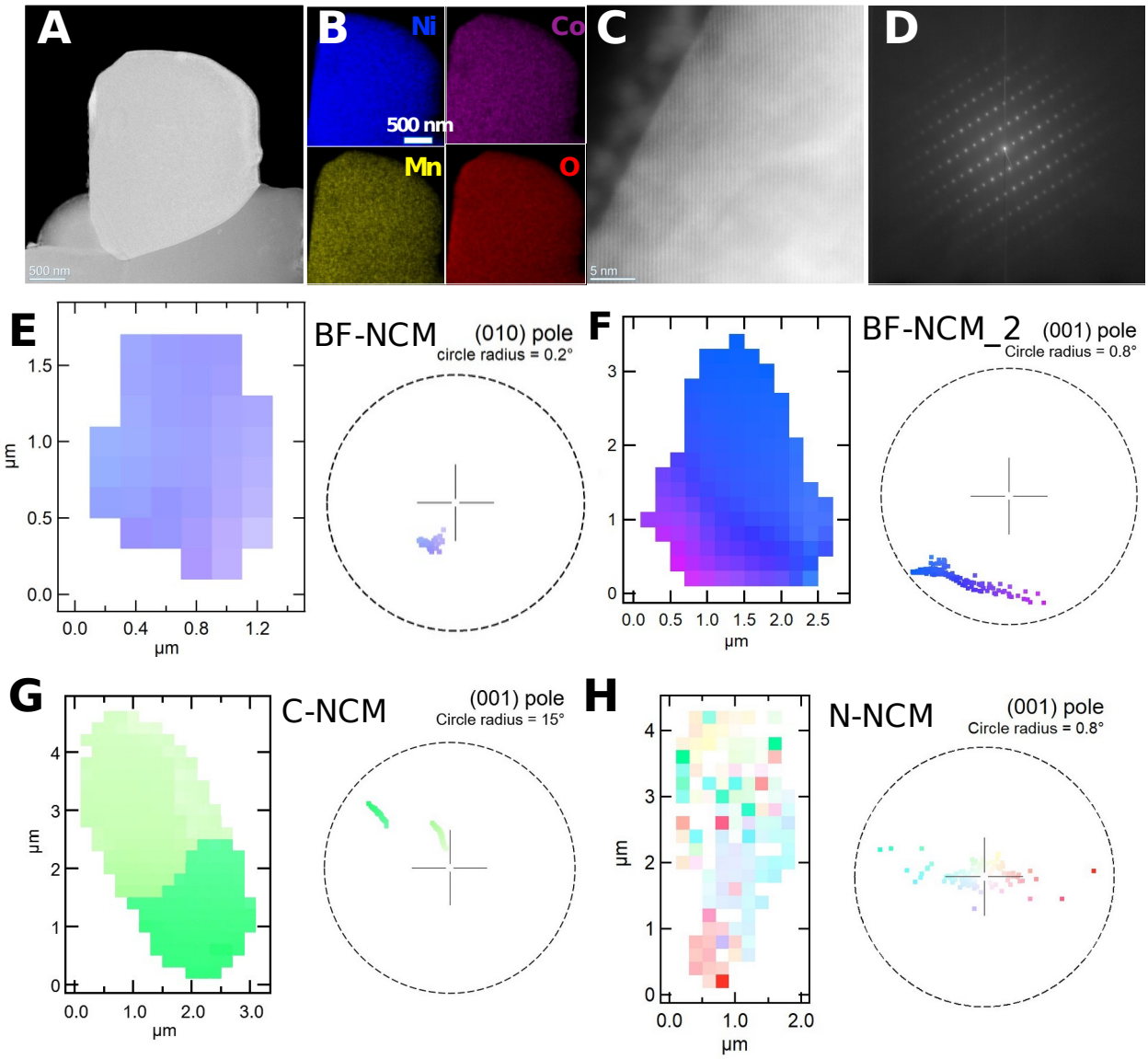

Fig. 1. Structure characterization of pristine cathodes. **(A)** HAADF-STEM image and **(B)** the corresponding elemental mapping of BF-NCM particle. **(C)** High-resolution HAADF-STEM image of BF-NCM particle. **(D)** 4D-STEM nanobeam diffraction pattern of **A**. Crystal orientation map of (**E**, **F**) BF-NCM, (**G**) C-NCM and (**H**) N-NCM measured by synchrotron Laue diffraction microscopy.

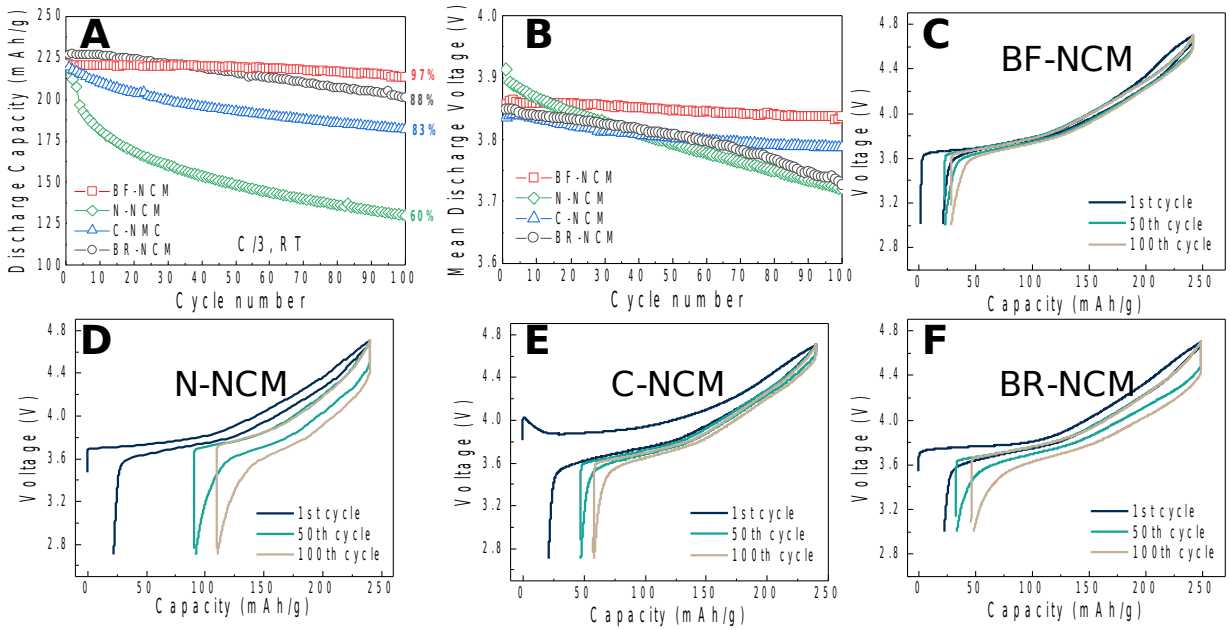

Fig. 2. Electrochemical performance of the investigated cathodes. (**A**) Cycling performance and (**B**) discharge mean voltage of NCM cathodes with different domain boundaries at C/3 with a charge cut-off voltage of 4.7 V. The corresponding voltage profiles of (**C**) BF-NCM, (**D**) N-NCM, (**E**) C-NCM and (**F**) BR-NCM.

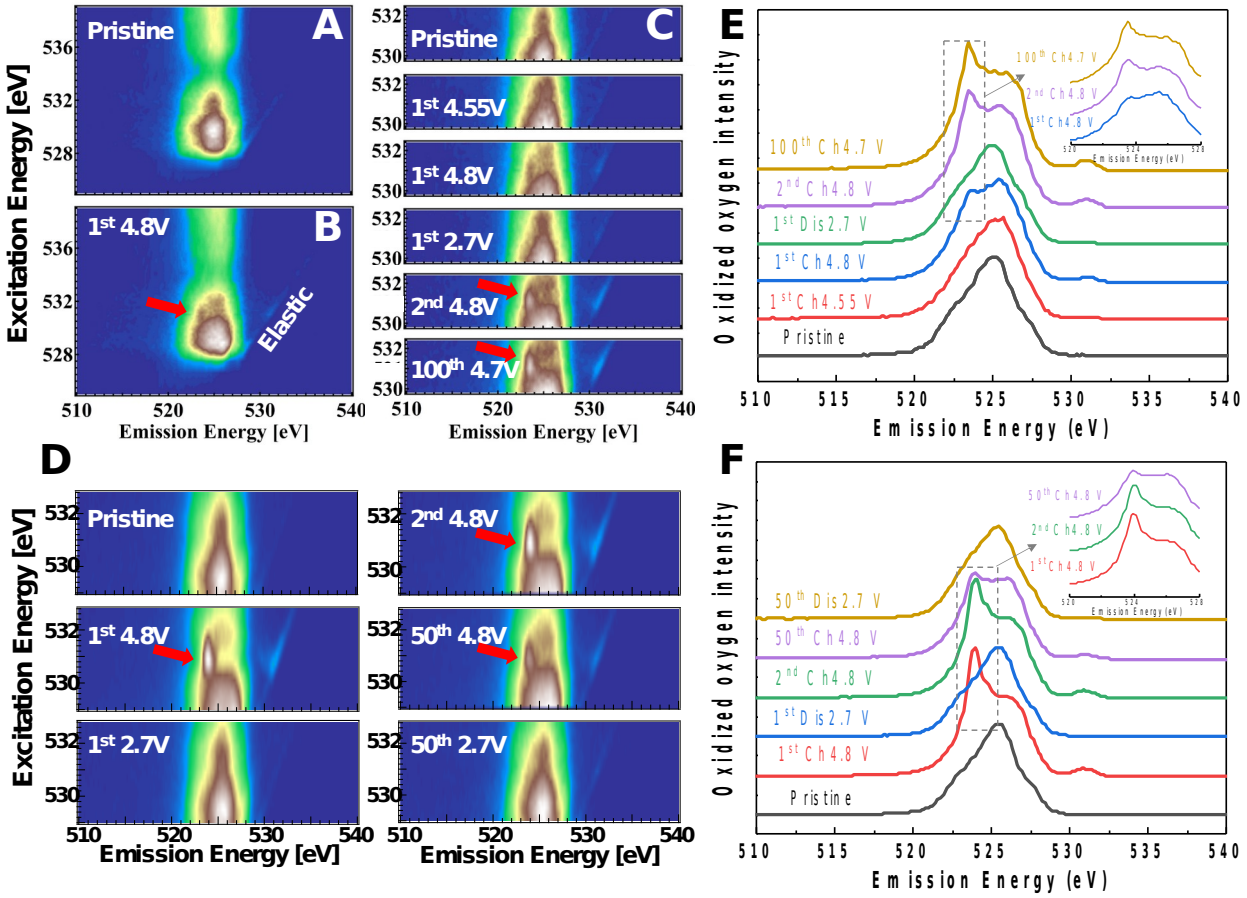

Fig. 3. O K-edge mRIXS characterization during cycling. The O K-edge mRXIS map of BF-NCM cathode at (**A**) pristine, (**B**) 1st 4.8V-charged state and (**C**) different charge/discharge states. (**D**) The O K-edge mRXIS map of C-NCM cathode at different charge/discharge states. Integrated RIXS intensity in the characteristic energy range of OR for (**E**) BF-NCM and (**F**) C-NCM cathode extracted by integrating the intensity with the characteristic excitation-energy range from 530.6 to 531.8 eV. Inset in (**E, F**) show the comparison on the charge state of different cycles.

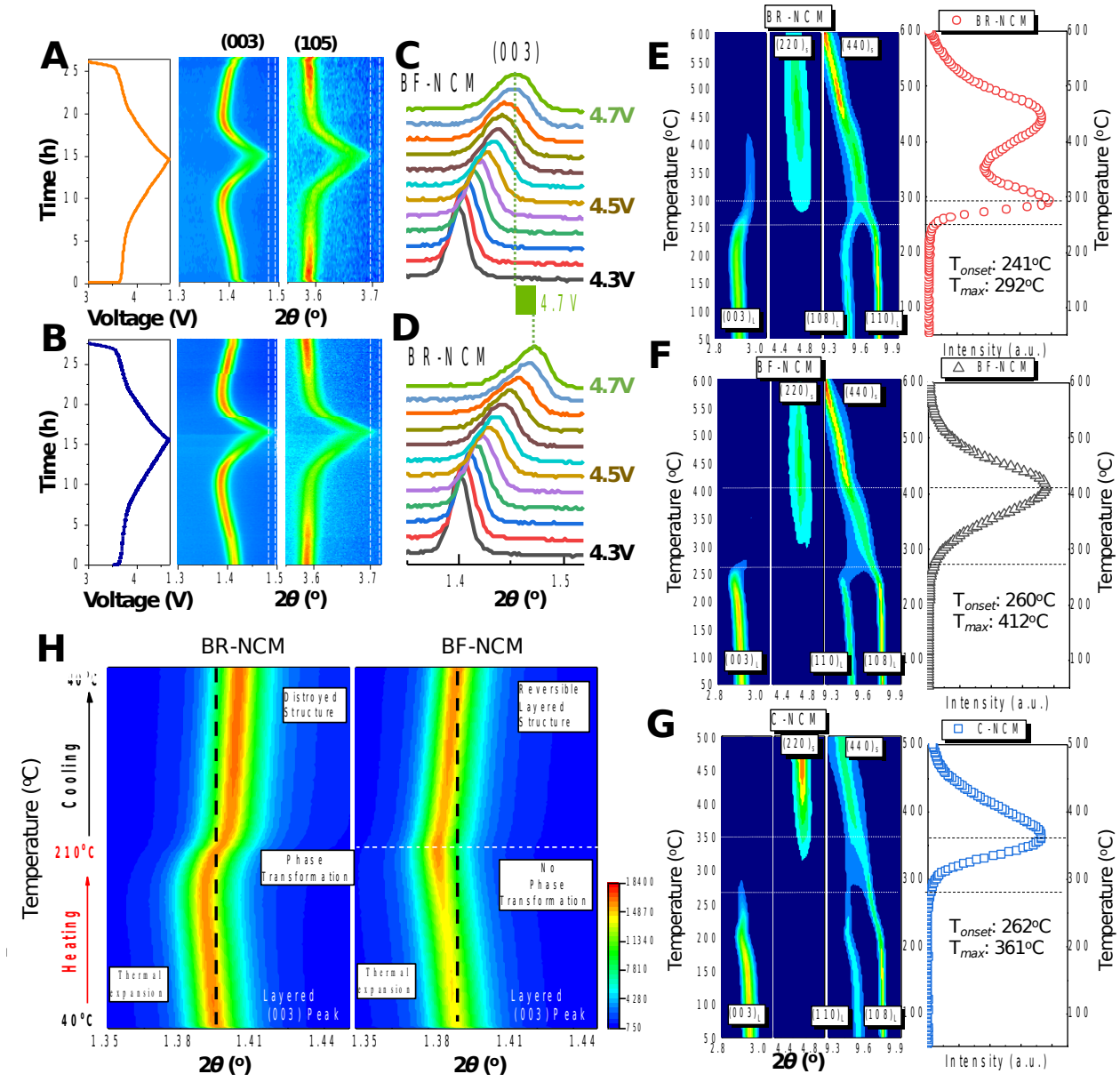

Fig. 4. In-situ synchrotron X-ray characterizations of cathodes. In-situ HEXRD of (**A**) BF-NCM and (**B**) BR-NCM cathodes during charge/discharge within 3.0-4.7 V at C/10. Zoom-in HEXRD patterns of (**C**) BF-NCM and (**D**) BR-NCM cathodes in the voltage region of 4.3-4.7 V. Contour images of in-situ HEXRD and oxygen evolution for charged (**E**) BR-NCM, (**F**) BF-NCM and (**G**) C-NCM cathodes during heating. **(H)** In-situ HEXRD of charged BF-NCM and BR-NCM cathodes during heating from 30 °C to 210 °C and then cooling back to 30 °C.

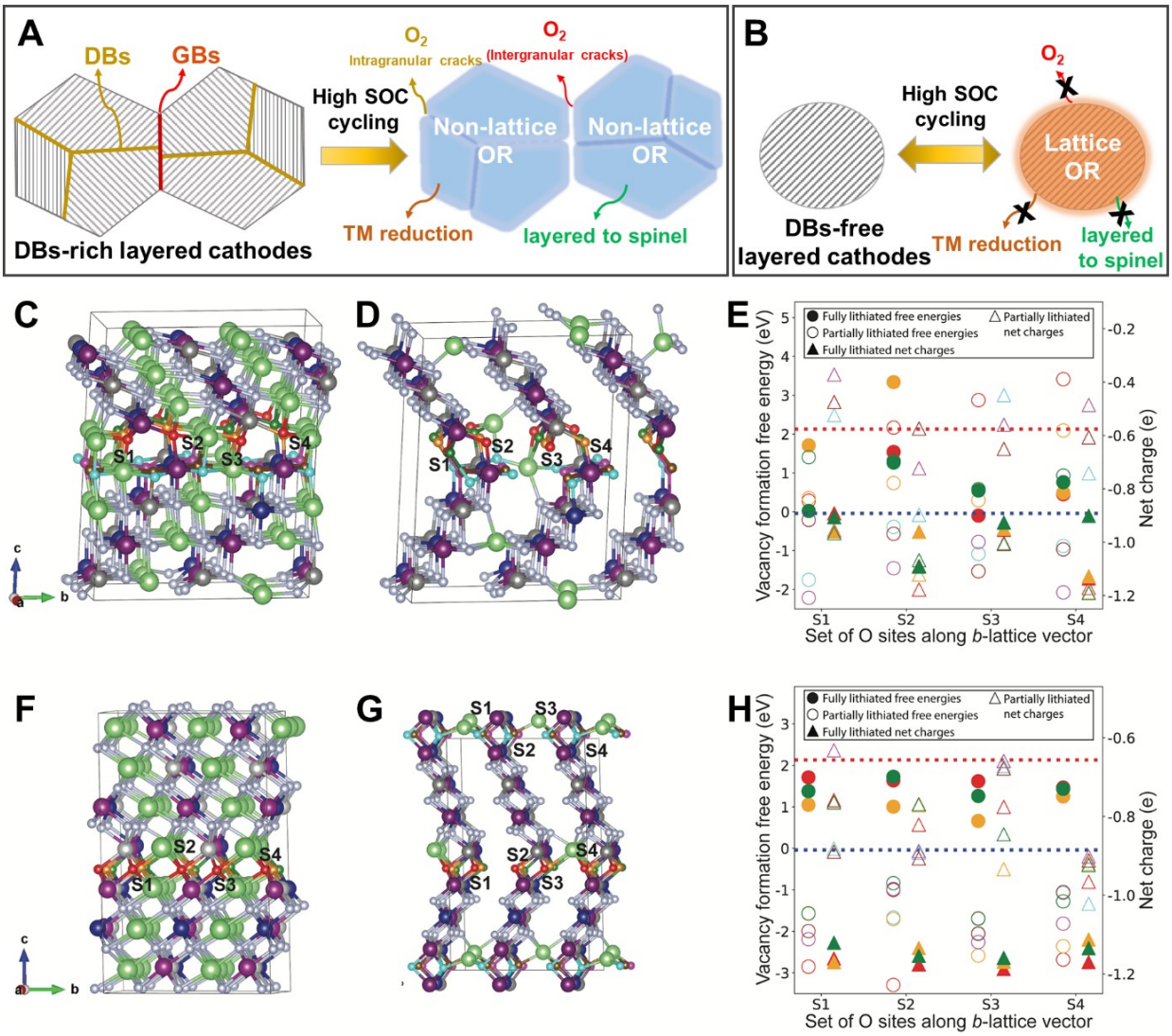

Fig. 5. Correlation between boundary structures and oxygen redox. (**A, B**) Schematic of oxygen redox activity of layered cathodes with respect to boundary structures. Simulated atomic structures of (**C**) fully lithiated $Li_3MnCoNiO_6$ and (**D**) partially lithiated $Li_{0.375}NiCoMnO_6$ with tilt boundary structure and the corresponding oxygen vacancy formation energy and net charge (**E**) of oxygen sites along *b*-lattice vector. Simulated atomic structures of (**F**) fully lithiated $Li_3MnCoNiO_6$ and (**G**) partially lithiated $Li_{0.357}NiCoMnO_6$ with twin boundary structure and the corresponding oxygen vacancy formation energy and net charge (**H**) of oxygen sites along *b*-lattice vector. Larger balls with green, blue, purple, and grey colour represent Li, Co, Mn and Ni atoms, respectively, while oxygen atoms at DBs were labelled by small balls with colour of red, orange, green, cyan, brown and magenta., oxygen atoms at the bulk are marked by white balls. The colour of oxygen atoms at different sites in E and H are consistent with those in C, D, F and G.

Reference

1 Reed, J. & Ceder, G. Role of Electronic Structure in the Susceptibility of Metastable Transition-Metal Oxide Structures to Transformation. *Chem. Rev.* **104**, 4513-4534 (2004).

2 McCalla, E. *et al.* Visualization of O-O peroxo-like dimers in high-capacity layered oxides for Li-ion batteries. *Science* **350**, 1516-1521 (2015).

3 Assat, G. & Tarascon, J.-M. Fundamental understanding and practical challenges of anionic redox activity in Li-ion batteries. *Nat. Energy* **3**, 373-386 (2018).

4 Luo, K. *et al.* Charge-compensation in 3d-transition-metal-oxide intercalation cathodes through the generation of localized electron holes on oxygen. *Nat. Chem.* **8**, 684-691 (2016).

5 Gent, W. E., Abate, I. I., Yang, W., Nazar, L. F. & Chueh, W. C. Design Rules for High-Valent Redox in Intercalation Electrodes. *Joule* **4**, 1369-1397 (2020).

6 Seo, D.-H. *et al.* The structural and chemical origin of the oxygen redox activity in layered and cation-disordered Li-excess cathode materials. *Nat. Chem.* **8**, 692-697 (2016).

7 House, R. A. *et al.* Superstructure control of first-cycle voltage hysteresis in oxygen-redox cathodes. *Nature* **577**, 502-508 (2020).

8 Pearce, P. E. *et al.* Evidence for anionic redox activity in a tridimensional-ordered Li-rich positive electrode β-Li_2IrO_3. *Nat. Mater.* **16**, 580-586 (2017).

9 Yabuuchi, N. *et al.* High-capacity electrode materials for rechargeable lithium batteries: Li_3NbO_4-based system with cation-disordered rocksalt structure. *Proc. Natl. Acad. Sci.* **112**, 7650-7655, (2015).

10 Perez, A. J. *et al.* Approaching the limits of cationic and anionic electrochemical activity with the Li-rich layered rocksalt Li_3IrO_4. *Nat. Energy* **2**, 954-962 (2017).

11 Maitra, U. *et al.* Oxygen redox chemistry without excess alkali-metal ions in $Na_{2/3}[Mg_{0.28}Mn_{0.72}]O_2$. *Nat. Chem.***10**, 288-295 (2018).

12 Rong, X. *et al.* Anionic Redox Reaction-Induced High-Capacity and Low-Strain Cathode with Suppressed Phase Transition. *Joule* **3**, 503-517 (2019).

13 Wu, J. *et al.* Dissociate lattice oxygen redox reactions from capacity and voltage drops of battery electrodes. *Sci. Adv.* **6**, eaaw3871 (2020).

14 Lee, E. & Persson, K. A. Structural and Chemical Evolution of the Layered Li-Excess Li_xMnO_3 as a Function of Li Content from First-Principles Calculations. *Adv. Energy Mater.* **4**, 1400498 (2014).

15 Kong, F. *et al.* Kinetic Stability of Bulk $LiNiO_2$ and Surface Degradation by Oxygen Evolution in $LiNiO_2$-Based Cathode Materials. *Adv. Energy Mater.* **9**, 1802586 (2019).

16 Yan, P. *et al.* Injection of oxygen vacancies in the bulk lattice of layered cathodes. *Nat. Nanotechnol.* **14**, 602-608 (2019).

17 Hu, E. *et al.* Evolution of redox couples in Li- and Mn-rich cathode materials and mitigation of voltage fade by reducing oxygen release. *Nat. Energy* **3**, 690-698 (2018).

18 Chen, Q. *et al.* Highly reversible oxygen redox in layered compounds enabled by surface polyanions. *Nat. Commun.* **11**, 3411 (2020).

19 Zhang, X.-D. *et al.* Suppressing Surface Lattice Oxygen Release of Li-Rich Cathode Materials via Heterostructured Spinel $Li_4Mn_5O_{12}$ Coating. *Adv. Mater.* **30**, 1801751 (2018).

20 Fan, X. *et al.* Crack-free single-crystalline Ni-rich layered NCM cathode enable superior cycling performance of lithium-ion batteries. *Nano Energy* **70**, 104450 (2020).

21 Li, J. *et al.* Comparison of Single Crystal and Polycrystalline $LiNi_{0.5}Mn_{0.3}Co_{0.2}O_2$ Positive Electrode Materials for High Voltage Li-Ion Cells. *J. Electrochem. Soc.* **164**, A1534-A1544 (2017).

22 Qian, G. *et al.* Single-crystal nickel-rich layered-oxide battery cathode materials: synthesis, electrochemistry, and intra-granular fracture. *Energy Storage Mater.* **27**, 140-149 (2020).

23 Bi, Y. *et al.* Reversible planar gliding and microcracking in a single-crystalline Ni-rich cathode. *Science* **370**, 1313-1317 (2020).

24 Zhang, F. *et al.* Surface regulation enables high stability of single-crystal lithium-ion cathodes at high voltage. *Nat. Commun.* **11**, 3050 (2020).

25 Xu, C. *et al.* Bulk fatigue induced by surface reconstruction in layered Ni-rich cathodes for Li-ion batteries. *Nat. Mater.* **20**, 84-92 (2021).

26 Zhu, J. & Chen, G. Single-crystal based studies for correlating the properties and high-voltage performance of $Li[Ni_xMn_yCo_{1-x-y}]O_2$ cathodes. *J. Mater. Chem. A* **7**, 5463-5474 (2019).

27 Klein, S. *et al.* Prospects and limitations of single-crystal cathode materials to overcome cross-talk phenomena in high-voltage lithium ion cells. *J. Mater. Chem. A* **9**, 7546-7555 (2021).

28 Han, Y., Heng, S., Wang, Y., Qu, Q. & Zheng, H. Anchoring Interfacial Nickel Cations on Single-Crystal $LiNi_{0.8}Co_{0.1}Mn_{0.1}O_2$ Cathode Surface via Controllable Electron Transfer. *Acs Energy Lett.* **5**, 2421-2433 (2020).

29 Pang, P. *et al.* Crack-free single-crystal $LiNi_{0.83}Co_{0.10}Mn_{0.07}O_2$ as cycling/thermal stable cathode materials for high-voltage lithium-ion batteries. *Electrochim. Acta* **365**, 137380 (2021).

30 Fan, X. *et al.* Unravelling the influence of quasi single-crystalline architecture on high-voltage and thermal stability of $LiNi_{0.5}Co_{0.2}Mn_{0.3}O_2$ cathode for lithium-ion batteries. *Chem. Eng. J.* **393**, 124709 (2020).

31 Li, N. *et al.* Unraveling the Cationic and Anionic Redox Reactions in a Conventional Layered Oxide Cathode. *Acs Energy Lett.* **4**, 2836-2842 (2019).

32 Lee, G.-H. *et al.* Reversible Anionic Redox Activities in Conventional $LiNi_{1/3}Co_{1/3}Mn_{1/3}O_2$ Cathodes. *Angew. Chem. Int. Ed.* **59**, 8681-8688 (2020).

33 Lee, S.-Y. *et al.* Revisiting Primary Particles in Layered Lithium Transition-Metal Oxides and Their Impact on Structural Degradation. *Adv. Sci.* **6**, 1800843 (2019).

34 Jiang, Y. *et al.* Atomistic mechanism of cracking degradation at twin boundary of $LiCoO_2$. *Nano Energy* **78**, 105364 (2020).

35 Ahmed, S. *et al.* Understanding the formation of antiphase boundaries in layered oxide cathode materials and their evolution upon electrochemical cycling. *Matter* **4**, 3953-3966 (2021).

36 Ge, M. *et al.* Kinetic Limitations in Single-Crystal High-Nickel Cathodes. *Angew. Chem. Int. Ed.* **60**, 17350-17355 (2021).

37 Geng, C. *et al.* Mechanism of Action of the Tungsten Dopant in LiNiO2 Positive Electrode Materials. *Adv. Energy Mater.* **12**, 2103067 (2022).

38 Yang, W. & Devereaux, T. P. Anionic and cationic redox and interfaces in batteries: Advances from soft X-ray absorption spectroscopy to resonant inelastic scattering. *J. Power Sources* **389**, 188-197 (2018).

39 Dai, K. *et al.* High Reversibility of Lattice Oxygen Redox Quantified by Direct Bulk Probes of Both Anionic and Cationic Redox Reactions. *Joule* **3**, 518-541 (2019).

40 Wu, J. *et al.* Fingerprint Oxygen Redox Reactions in Batteries through High-Efficiency Mapping of Resonant Inelastic X-ray Scattering. *Condens. Matter.* **4**, 5 (2019).

41 Zhuo, Z. *et al.* Spectroscopic Signature of Oxidized Oxygen States in Peroxides. *J. Phys. Chem. Lett.* **9**, 6378-6384 (2018).

42 Yang, W. Oxygen release and oxygen redox. *Nat. Energy* **3**, 619-620 (2018).

43 Liu, X. *et al.* Probing the Thermal-Driven Structural and Chemical Degradation of Ni-Rich Layered Cathodes by Co/Mn Exchange. *J. Am. Chem. Soc.* **142**, 19745-19753 (2020).

44 Rana, J. *et al.* Structural Changes in Li_2MnO_3 Cathode Material for Li-Ion Batteries. *Adv. Energy Mater.* **4**, 1300998 (2014).

45 Li, W., Asl, H. Y., Xie, Q. & Manthiram, A. Collapse of $LiNi_{1-x-y}Co_xMn_yO_2$ Lattice at Deep

Charge Irrespective of Nickel Content in Lithium-Ion Batteries. *J. Am. Chem. Soc.* **141**, 5097-5101 (2019).

46 Kondrakov, A. O. *et al.* Charge-Transfer-Induced Lattice Collapse in Ni-Rich NCM Cathode Materials during Delithiation. *J. Phys. Chem. C* **121**, 24381-24388 (2017).

47 Xu, C., Reeves, P. J., Jacquet, Q. & Grey, C. P. Phase Behavior during Electrochemical Cycling of Ni-Rich Cathode Materials for Li-Ion Batteries. *Adv. Energy Mater.* **11**, 2003404 (2021).

48 Ren, D. *et al.* Model-based thermal runaway prediction of lithium-ion batteries from kinetics analysis of cell components. *Appl. Energy* **228**, 633-644 (2018).

49 Yun, J. S. *et al.* Critical Role of Grain Boundaries for Ion Migration in Formamidinium and Methylammonium Lead Halide Perovskite Solar Cells. *Adv. Energy Mater.* **6**, 1600330 (2016).

50 Polfus, J. M., Yildiz, B. & Tuller, H. L. Origin of fast oxide ion diffusion along grain boundaries in Sr-doped $LaMnO_3$. *Phys. Chem. Chem. Phys.* **20**, 19142-19150 (2018).

51 Qiao, R. *et al.* High-efficiency in situ resonant inelastic x-ray scattering (iRIXS) endstation at the Advanced Light Source. *Rev. Sci. Inst.* **88**, 033106 (2017).

52 Chuang, Y.-D. *et al.* Modular soft x-ray spectrometer for applications in energy sciences and quantum materials. *Rev. Sci. Inst.* **88**, 013110 (2017).

53 Hu, E. *et al.* Oxygen-redox reactions in $LiCoO_2$ cathode without O–O bonding during charge-discharge. *Joule* **5**, 720-736 (2021).

54 Deng, J. *et al.* The Velociprobe: An ultrafast hard X-ray nanoprobe for high-resolution ptychographic imaging. *Rev. Sci. Inst.* **90**, 083701 (2019).

55 Wakonig, K. *et al.* PtychoShelves, a versatile high-level framework for high-performance analysis of ptychographic data. *J. Appl. Crystallogr.* **53**, 574-586 (2020).

56 Pelt, D. M. *et al.* Integration of TomoPy and the ASTRA toolbox for advanced processing and reconstruction of tomographic synchrotron data. *J. Synchrotron Radiat.* **23**, 842-849 (2016).

57 E. Schwenker et al., Ingrained: An automated framework for fusing materials imaging simulations into experiments (2021)*; https://github.com/MaterialEyes/ingrained-lite*.

58 He, X., Sun, H., Ding, X. & Zhao, K. Grain Boundaries and Their Impact on Li Kinetics in Layered-Oxide Cathodes for Li-Ion Batteries. *J. Phys. Chem. C* **125**, 10284-10294 (2021).

59 Jain, A. *et al.* A high-throughput infrastructure for density functional theory calculations. *Comput. Mater. Sci.* **50**, 2295-2310 (2011).

60 Jain, A. *et al.* Formation enthalpies by mixing GGA and GGA $+$ U calculations. *Phys. Rev. B* **84**, 045115 (2011).

61 Gale, J. D. GULP: A computer program for the symmetry-adapted simulation of solids. *J. Chem. Soc. Faraday Trans.* **93**, 629-637 (1997).

62 Kresse, G. & Furthmüller, J. Efficiency of ab-initio total energy calculations for metals and semiconductors using a plane-wave basis set. *Comput. Mater. Sci.* **6**, 15-50 (1996).

63 Kresse, G. & Furthmüller, J. Efficient iterative schemes for ab initio total-energy calculations using a plane-wave basis set. *Phys. Rev. B* **54**, 11169-11186 (1996).

64 Blöchl, P. E. Projector augmented-wave method. *Phys. Rev. B* **50**, 17953-17979 (1994).

65 Kresse, G. & Joubert, D. From ultrasoft pseudopotentials to the projector augmented-wave method. *Phys. Rev. B* **59**, 1758-1775 (1999).

66 Henkelman, G., Arnaldsson, A. & Jónsson, H. A fast and robust algorithm for Bader decomposition of charge density. *Comput. Mater. Sci.***36**, 354-360 (2006).

67 Wang, L., Maxisch, T. & Ceder, G. Oxidation energies of transition metal oxides within the $\mathrm{GGA}+\mathrm{U}$ framework. *Phys. Rev. B* **73**, 195107 (2006).

68 NIST Chemistry WebBook, NIST Standard Reference Database Number 69, Eds. P.J. Linstrom and W.G. Mallard, National Institute of Standards and Technology, Gaithersburg MD, 20899*, https://doi.org/10.18434/T4D303, (retrieved April 20, 2021).*